A comparative study of microstructures and nanomechanical properties of additively manufactured and commercial metallic stents

Langi, E.; Zhao, L. G.; Jamshidi, P.; Attallah, M.; Silberschmidt, V. V.; Willcock, H.; Vogt, F.

DOI:
10.1016/j.mtcomm.2022.103372

A Comparative Study of Microstructures and Nanomechanical Properties of Additively Manufactured and Commercial Metallic Stents

E Langi[a], LG Zhao[a*], P Jamshidi[b], M Attallah[b], VV Silberschmidt[a], H Willcock[c], F Vogt[d]

[a]Wolfson School of Mechanical, Electrical and Manufacturing Engineering and [c]Department of Materials, Loughborough University, Epinal Way, Loughborough, LE11 3TU, UK

[b]School of Metallurgy and Materials, University of Birmingham, Edgbaston, Birmingham, B15 2TT, UK

[d]Medical Clinic I, RWTH University Hospital Aachen, Pauwelsstrasse 30, 52074 Aachen, Germany

*Corresponding author. E-mail: L.Zhao@Lboro.ac.uk; Tel.: 0044-1509-227799.

Abstract

Additive manufacturing emerges as an innovative technology to fabricate medical stents used to treat blocked arteries. However, there is a lack of direct comparative study of the underlying microstructure and mechanical properties of additively manufactured and commercial stents. In this study, additively manufactured and commercial 316L stainless steel stents were studied comparatively, including electrochemical polishing to improve the surface finish of the additively manufactured stent. Microstructural characterisation was carried out through optical microscopy, scanning electron microscopy, and electron backscatter diffraction. Hardness and elastic modulus were studied using nanoindentation, with an emphasis on the effect of grain orientation. Furthermore, spherical nanoindentation was performed to extract the indentation stress-strain curve from the load-displacement data. Results showed that electrochemical polishing was effective in reducing the average surface roughness, with a reduction of Ra value from 9.04 μm to 1.53 μm. The microstructure of the additively manufactured stent consisted of hierarchical grain microstructure with columnar grains and cellular sub-grains, as opposed to equiaxed fine grains

and twins in the commercial stent. The hardness and modulus of the as-built stent were higher than those of the commercial stent. The grains close to the (111) orientation exhibited the highest hardness and elastic modulus followed by (101) and then (001) orientations. The indentation stress-strain curves, yield strength, and hardening behaviour were similar for the additively manufactured and commercial stents. This work provides a fundamental understanding of the microstructure and properties of the additively manufactured stent and represents an important step towards innovative manufacturing of stents.

Keywords: Additive manufacturing; Metallic stents; Selective laser melting; Material microstructure; Mechanical properties; Nanoindentation

1. Introduction

Cardiovascular diseases (CVDs) are the main cause of mortality globally, contributing to 30% of all deaths. While 85% of all CVDs are associated with heart attack and strokes caused by blocked arteries. Stent implantation has become one of the standard medical procedures to treat blocked arteries, with over 1 million procedures performed annually in Europe alone. In this procedure, the vessel capacity is restored by inflating a stent with a balloon to maintain the lumen open after the intervention. Development of stents went through the stages of bare-metal stents (BMSs), drug-eluting stents (DESs), and bioresorbable stents (BRSs); as of today, thin-strut DESs, made of metallic alloys such as Co-Cr alloy and coated with drugs, remain as the gold standard for treating patients with severely blocked arteries. This is largely because of their superiority in preventing in-stent restenosis, i.e., re-narrowing of the blood vessel due to intima hyperplasia, and late stent thrombosis which is associated with less biocompatible materials and bulky struts such as polymeric BRSs.

Currently, stents are laser machined from seamless microtubes; followed by surface finishing through acid pickling and electrochemical polishing to remove the heat-affected zone left by laser cutting. The use of standard microtubes during laser micromachining results in vascular stents with a uniform design, in terms of diameter, length and design. However, the diameter and shape of diseased arteries differ considerably from patient to patient, and the stents with uniform designs are difficult to produce desirable outcomes. Hence, there is a clear clinical need to manufacture patient-specific stents which cannot be realised via traditional tube laser machining. With the use of magnetic resonance imagining (MRI) and computed tomography (CT) for pre-surgical assessment and the emerging additive manufacturing (AM) technology, cardiovascular stents with personalised designs can be produced to revolutionise the treatment of patients with CVDs.

Recently, AM has been investigated as an alternative method for producing polymeric stents for medical applications. Guerra *et al.*, 2018 used 3D printing to produce polycaprolactone (PCL) stents with 200 μm strut size and 5 mm diameter. They studied the effect of process parameters on the physical features of stents, confirming the potential of producing polymeric stents using AM. AM gave an average dimensional accuracy between 80% and 90%, with controllable effects on the structure of the printed stent. All the stents showed good radial behaviour with an average radial expansion of 320% and an average recoil of 22.78%. While, Moore *et al.*, 2016 printed a lesion-specific poly-propylene stent with an average strut size of 400 μm and reported that there were inherent weaknesses in the printed stent due to the layer-by-layer build mechanism. When the stent was expanded, the strut failed due to linear delamination along the z-plane (vertical axis). The authors also acknowledged the challenge of printing a polymeric stent with a strut thickness of less than 200 μm. Jia *et al.*, (2018) printed a self-expanding vascular stent from polylactide (PLA) with 4 mm diameter, 40 mm length and 400 μm strut size. Results revealed that the printed stent could be compressed to a smaller diameter for ease of implantation. Further, the compressed stent showed excellent shape flexibility and maintained its shape at room temperature. These studies

have also shown that polymeric stents were significantly softer than metallic stents, which affected the radial stiffness of the implanted stent (Bünger *et al.*, 2007). Polymeric stents generally have weak mechanical properties, and therefore difficult to maintain structural and functional integrity after deployment. Hence, there is a growing need to produce metallic stents using AM via selective laser melting (SLM).

Over the past few years, great efforts have been made to manufacture metallic stents via SLM. where successive layers (typically 20-50 μm) of metallic powders are selectively melted using a laser beam as an energy source to produce the desired geometry according to the CAD profile. Wessarges *et al.*, used a fine powder in the range of 5-20 μm and a micro-SLM machine to produce 316L stainless steel prototype stents (Wessarges *et al.*, 2014). They were able to produce stents with a diameter of 2 mm and minimum and maximum strut thickness of 50 and 100 μm. After the manufacturing process, plasma polishing was used to remove the unmelted metallic powders followed by chemical polishing, resulting in smoothed stent surfaces and decreased strut thickness. The elastic recoil for all the stents was in the range of 3.2 to 6.5 % and the radial stiffness was in the range of 0.05 to 0.26 MPa, respectively. The change in length after stent expansion was in the range of -22 and -25%, implying that the printed stents did not meet the recommended change in length smaller than 1% for a conventional stent (Schmidt *et al.*, 2002). Generally, the prototype stents showed promising mechanical performance despite the observed micro-cracks close to the strut junction after expansion. Demir *et al.,* (2017) investigated the manufacturing of CoCr stents via SLM (Demir and Previtali, 2017). In their study, they outlined rules on creating self-supporting geometry when printing stents, which was to ensure that there is no unnecessary damage to the stent when removing supports after printing. Further, they proposed that struts at angles greater than 45° to the horizontal should overhang less than 1 mm, and the minimum gap between struts must be higher than 0.3 mm to guarantee that the struts do not merge. They designed a stent in CAD with a 200 μm strut thickness, while the printed stents had a strut thickness in the range of

250 to 380 μm, indicating the challenge of AM of stents. They also revealed that electrochemical polishing was effective in reducing the average surface roughness, i.e., from 9.19 to 1.45 μm which represents a ~85 % reduction. Further, the microhardness on the strut cross-section was in the range of 320 and 400 HV, similar to those reported in the literature (Zhou *et al.*, 2015). Finazzi *et al.*, (2020) produced CoCr prototype stents using SLM with strut sizes in the range of 90 and 120 μm. Results revealed that there were no macro-defects detected in the manufactured stents and electrochemical polishing was used to improve the surface quality of the stent by reducing the average roughness from 8.4 μm to 2.2 μm. Mechanical properties were also evaluated on a printed mini-dog bone sample with a width similar to the stent strut thickness. The elastic modulus, yield strength, ultimate tensile strength, and corresponding strain at failure were 60.4 GPa, 376.5 MPa, 694.0 MPa, and 9.9 %, respectively, which were comparable to conventional CoCr alloy. Stent expansion study showed that the internal diameter of the stent increased twice the original value, and SEM examinations did not show any cracks after expansion. Clearly, AM of stents was proved plausible in literature, but the full potential of producing metallic stents through SLM is yet to be discovered, especially a direct comparison with a commercial stent with regards to the microstructure and its connection with mechanical properties, which are essential for the commercialisation of the technology.

The aim of this work was therefore to comparatively investigate the microstructure and mechanical properties of SLMed and commercial 316L stainless steel stents. Firstly, electrochemical polishing was carried out to improve the surface quality of printed stents, followed by characterisation using optical microscopy (OM) and scanning electron microscopy (SEM)/electron backscatter diffraction (EBSD). The mechanical properties such as hardness and Young's modulus were measured using a sharp indenter tip (Berkovich). To further understand the elastic-plastic behaviour of the stent, the indentation stress-strain curve was extracted from the load-displacement curve using a blunt spherical indenter tip. A full comparison with a commercial stent

was conducted, which is critical for evaluating the potential of additive manufacturing in stent fabrication.

2. Material and methodologies

2.1. Material

The material studied here is 316L stainless steel (SS) which has been used for manufacturing metallic stents since the beginning of stent technology in the 1980s. Both SLMed and commercial 316L SS stents were investigated in this study, and they are referred to *as-built* and *commercial stents,* respectively. The as-built stent was produced by SLM using a Concept Laser M2 cusing system. They were built on a steel substrate in an Argon atmosphere where oxygen content was less than 100 ppm. The M2 system has a Yb-fibre laser, with a laser power up to 400 W, a laser spot size of 60 μm, a track width of 150 μm, and a scan speed up to 7000 mm/s. The 316L SS powder supplied by Atomising Systems Ltd (Sheffield, UK) was used as a feedstock material, with an average size of 32 μm (distributed between 15 and 53 μm). The stent was built using a laser power of 100 W, a layer thickness of 20 μm, and a scan speed of 1600 mm/s. The as-built stent had a Palmaz-Schatz design, with a diameter of 5 mm, a height of 13.64 mm, and a strut thickness of 360 μm. The commercial stent was Multi-Link RX Ultra™ made by Abbott, with a strut size of 100 μm and a diameter of 3 mm in an expanded state. It was produced by laser micromachining of a thin-walled tube. Figure 1 shows the as-built and commercial stents used in this study.

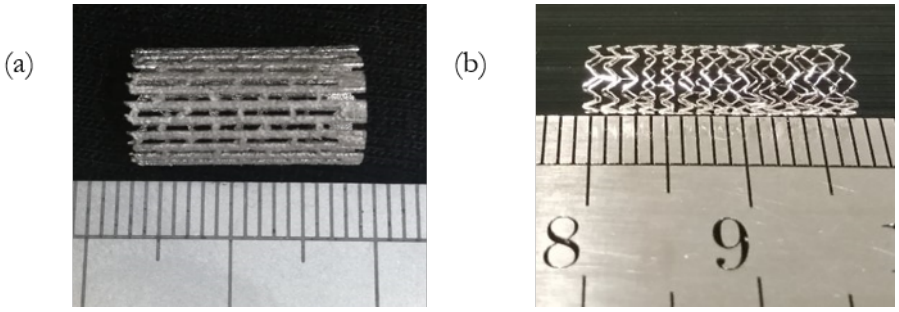

Fig. 1 (a) As-built stent with a strut thickness of 360 μm; (b) commercial stent with a strut thickness of 100 μm.

2.2 Electrochemical polishing

Commercial stents produced by laser micromachining of the thin-walled tube are normally finished with electrochemical polishing. Here, the same method was applied to the as-built stent to improve the surface quality. Before electrochemical polishing, acid pickling was first performed to remove surface oxides and other contaminants from the SLMed stent by immersion in an aqueous acid solution containing 3 ml hydrofluoric acid, 9 ml nitric acid, and 88 ml water. Pickling was done at room temperature for 3 mins, and the stent was then cleaned in an ultrasonic agitation bath for 5 min and dried in air. Next, electrochemical polishing was conducted to the stent in an electrolyte bath. The electrolyte solution was composed of 42 ml phosphoric acid (H_3PO_4), 47 ml Glycerol, and 11 ml water. The temperature was kept at 75°, and the applied voltage and current were 12 V and 1.2 A, respectively. The total immersion time was set as 1.5 min and divided into 3 steps, each having a duration of 30 s. In between the immersion steps, the as-built stents were cleaned by ultrasonication in ethyl alcohol and dried in air.

2.3 Surface characterisation

The surface roughness was characterised using the focus variation technique by Alicona Infinite, which combines a small depth of focus of an optical system with vertical scanning to produce a topographic model of the surface. In this study, a 10× objective lens was used, with a 1.4 mm × 1.0 mm field of view, a 2 μm lateral resolution, a 17 mm stand-off distance, and a 1 μm vertical resolution. The obtained roughness parameters included average roughness Ra, root-mean-square Rq, and the mean roughness depth Rz.

2.4. XRD analysis

X-ray diffraction (XRD) was used to characterise the phase content of the stents, using a Bruker D8 X-ray diffractometer. The diffractometer used Cu-Kα radiation and operated at a voltage of 30 kV and a current of 10 mA. The 2θ was varied from 30° to 120° and a scan was performed at a step size of 0.02° per minute. The diffraction patterns obtained were plotted as intensity against 2θ. The JCPDS-cards 31-0619 and 06-0696 were used for the identification of different phases in the samples. In addition, the Williamson and Hall method was used to evaluate dislocation density from XRD results (Yin *et al.*, 2019).

2.5 Microstructure characterisation

The cross-sectional microstructures of the samples were studied using an optical microscope (Zeiss Primotech) and a field emission scanning electron microscope (SEM JEOL 7800). The samples for metallographic examination were cut and cold mounted in epoxy resin. Next, the samples were ground with 1200 grit silicon carbide paper followed by a polishing procedure using diamond pastes of 9, 3, and 1 µm, successively. The final polishing was with 0.05 µm colloidal silica suspension using Buehler VibroMet™ 2 to improve the polishing quality. For optical microscopy and SEM examinations, the polished samples were chemically etched in a carpenter etchant solution (8.5 g $FeCl_3$, 2.4 g $CuCl_2$, 122 ml HCl, 6 ml HNO_3, and 122 ml $C_2H_{76}O$) for 30 s to reveal the grain structure. Energy Dispersive Spectroscopy (EDS) affiliated to the SEM was performed on the SLMed stent to detect micro-segregation. The grain morphology was analysed by EBSD system on the SEM JEOL 7800 equipped with an Oxford Nordlys II S EBSD detector. The sample was tilted to 70° and a working distance of 10 mm was maintained. All measurements were performed with an acceleration voltage of 20-kV and a 1.5 µm step size. The acquired EBSD maps were further processed by removing wild spikes and reducing minor noise (using 7 nearest neighbours). HKL channel 5 data processing software was used to generate inverse pole figure

(IPF) maps and carry out a detailed analysis of grain size and distribution. The grain size was estimated by calculating the diameter of a circle with an equal grain surface area.

2.6 Nanoindentation

Further to the microstructural investigations, nanoindentation was performed at different load levels to extract mechanical properties using both Berkovich and spherical indenter tips. Samples for indentation were metallographically ground and polished, with the final stage of polishing performed using a colloidal silica suspension. All tests were performed on a NanoTest Platform 3 machine (Micromaterials). Prior to the tests, the indenter tip area function was calibrated by performing indentations on a standard specimen of fused silica, where the tip has an elastic modulus of 1140 GPa and a Poisson's ratio of 0.07.

2.6.1 Berkovich nanoindentation

The behaviour and mechanical properties such as hardness and elastic modulus of the stents were analysed with Berkovich indenter tip. Load-controlled indentations were performed using five different load levels of 3, 7, 10, 15, and 25 mN. The loading and unloading times were 10 s, and a 10 s dwell time was imposed at the peak load. For this test, 16 indentations were performed at each load level. Oliver and Pharr's methods (Oliver and Pharr, 1992) were used to calculate the hardness, H, and effective Young's modulus, E_{eff}, after a complete loading-unloading cycle. To study the effect of grain orientation on hardness and the Young's modulus, EBSD was performed after nanoindentation. For this calculation, three crystallographic orientations i.e. (001), (101), and (111) were considered. At each indentation point, orientation in terms of Bunge–-Euler angles were extracted using the HKL Channel 5.0 EBSD post-processing software.

2.6.1 Spherical nanoindentation

The behaviour of the stents was further assessed using a 10-µm blunt spherical indenter tip to extract stress-strain responses. For this test, 20 loading–unloading indentation cycles were conducted on the samples. The protocols used in this study to extract the indentation stress-strain curves from the load-displacement data followed the work by Kalidindi *et al.,* (Pathak, Shaffer and Kalidindi, 2009; Pathak and Kalidindi, 2015; Patel and Kalidindi, 2016) which are based on the Hertz theory. Specifically, the values of indentation stress and strain can be calculated by recasting Hertz theory for spherical indentation as

$$\sigma_{ind} = \frac{P}{\pi a^2}, \qquad \varepsilon_{ind} = \frac{4}{3\pi}\frac{h_t}{a} \approx \frac{h_t}{2.4a} \tag{1}$$

where P, a, σ_{ind}, ε_{ind}, E_{eff} are the load, contact radius, indentation stress, indentation strain, and effective modulus. From each measured indentation–stress-strain curve (equation 1), the indentation elastic modulus and the indentation yield strength were also extracted. Here, a 0.2% offset strain was employed to identify the indentation yield strength.

3. Results and discussions

3.1. Surface roughness

The as-built stent, shown in Fig. 1(a), had a high surface roughness, a typical characteristic of parts produced by SLM. As a starting point, pickling and electrochemical polishing were conducted for the SLMed stent. Table 1 presents the weight and weight loss of the as-built, pickled, and polished stent. The as-built stent weighed about 498.24 mg. After pickling in an aqueous acid solution, the weight was reduced to 487.80 mg, representing a 2.1% weight loss. After electrochemical polishing, the weight of the stent was further reduced to 478.40 mg, resulting in a weight loss of 1.9 %.

Table 1: Weight and weight losses of the stent before and after electrochemical polishing

	Sample	Weight (mg)	Weight loss (%)
As-built stent	Received	498.24	~
	Pickled	487.80	2.1
	Polished	478.40	1.9

The SEM images of the as-built, pickled/electropolished, and commercial stents are shown in Fig. 2 (a), (b), and (c), respectively. In the as-built condition, the surface showed typical features of the SLM process, such as sintered particles and solidified melt-pools. It was observed that a smooth surface was obtained after pickling and electrochemical polishing processes. Clearly, pickling, and electrochemical polishing allowed the removal of sintered particles without excessively altering the cell structure (see Fig. 2(b)), but still considerably rougher than the commercial stent (Fig. 2c).

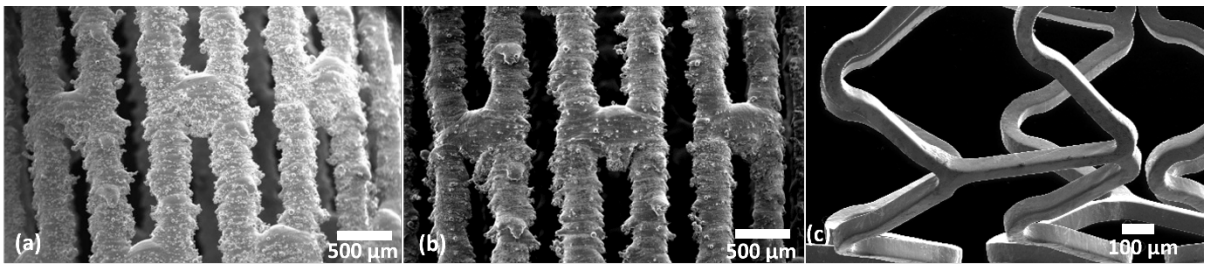

Fig. 2. SEM image of the (a) as-built, (b) electropolished, and (c) commercial stents.

The surface roughness of the as-built, electropolished and commercial stents were measured using the focus variation technique. Figs. 3 (a), (b), and (c) show surface morphology of the struts in the as-built condition, after electrochemical polishing and for the commercial stent, respectively. With electrochemical polishing, all the sintered particles were removed, and the surface quality was significantly improved, although still poorer than the commercial stents.

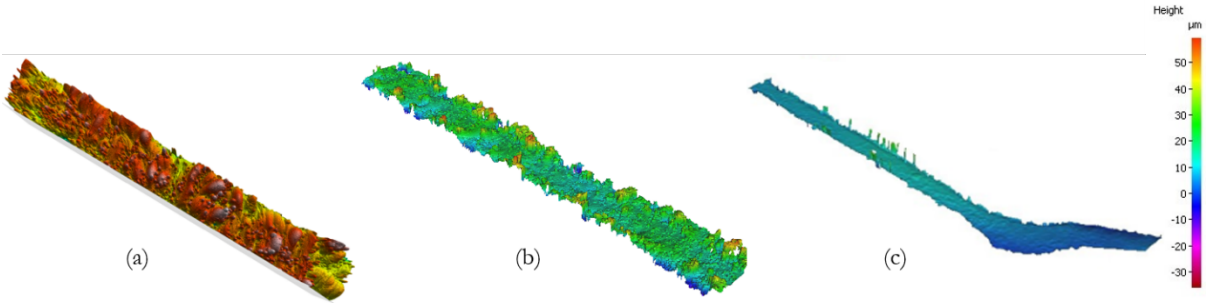

Fig.3. Surface morphology of the (a) as-built, (b) electropolished and (c) commercial stents.

Fig. 4 reports the surface roughness parameters for the as-built, electropolished and commercial stents conditions. Specifically, the average roughness Ra, the root mean square roughness Rq, and the mean roughness depth Rz for the as-built stent decreased from 9.04 µm to 1.53 µm; 11.68 µm to 2.34 µm, and 57.52 µm to 7.80 µm, respectively, after electrochemical polishing; demonstrating a significant reduction (by ~83%) in surface roughness. However, further reduction of Ra is required to achieve the surface finish required for medical application i.e. Ra<0.5 µm (Finazzi *et al.*, 2020). The surface roughness of the printed stent can be improved further using more effective etching solutions such as 95-97 % H_2SO_4, 85 wt% H_3PO_4 and H_2O. In addition, the combination of mechanical polishing (e.g. grinding) with electro and plasma polishing and blasting using different grits has also been reported to improve the surface quality significantly (Löber *et al.*, 2013). On the other hand, the roughness parameters for the commercial stent were 0.18, 0.26, and 1.23 µm, respectively, well below the recommended value for medical application.

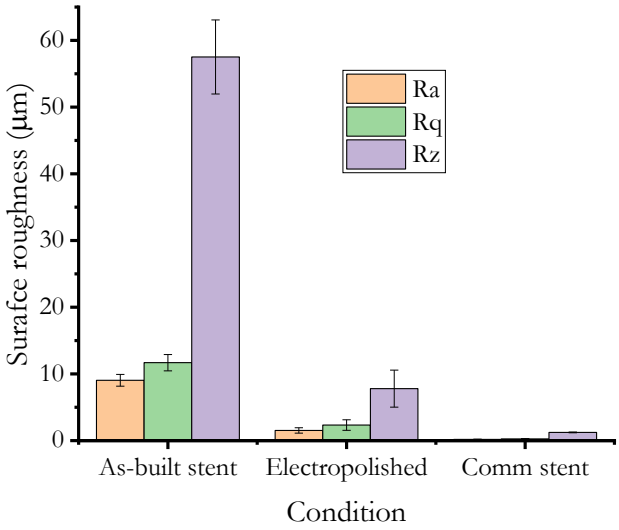

Fig. 4. Average roughness (Ra), root mean square roughness (Rq), and mean roughness depth (Rz) of SLMed stents in the as-built and electropolished conditions; in comparison with those for a commercial stent.

3.2 XRD analyses

Fig. 5 presents the XRD plot for the as-built and commercial stents. The recorded XRD patterns had numerous sharp peaks, in a good match with the face-centered-cubic (FCC) austenite phase. In addition, the results of XRD analyses of the as-built stent revealed the presence of a secondary phase such as ferrite. On the other hand, the XRD pattern for commercial stents showed traces of the third phase such as δ-phase in addition to austenite and ferrite phases. Other studies (Saeidi, Gao, Lofaj, *et al.*, 2015; Langi *et al.*, 2020) reported the formation of single-phase austenite in SLMed 316L SS samples and attributed this to a high cooling rate. While Saeidi *et al. (year?)* reported the formation of a second phase (ferrite) after conducting heat treatment at 1100°C for one hour followed by furnace cooling and attributed this to solute partitioning.

The difference in the relative intensities of stents indicated the presence of crystallographic texture in the as-built stent with preferential growth. Using the Williamson–Hall method, internal strain

(ε) for the as-built and commercial stents was calculated to be 0.176% and 0.099%, respectively. The dislocation density for the printed stent and commercial stent was estimated to be $7.68\times10^{14}\ m^{-2}$ and $2.44\times10^{14}\ m^{-2}$, respectively. Furthermore, the peaks for the as-built stent were broader compared to those of commercial stent, as a result of the presence of high internal strains and dislocations introduced during the SLM process.

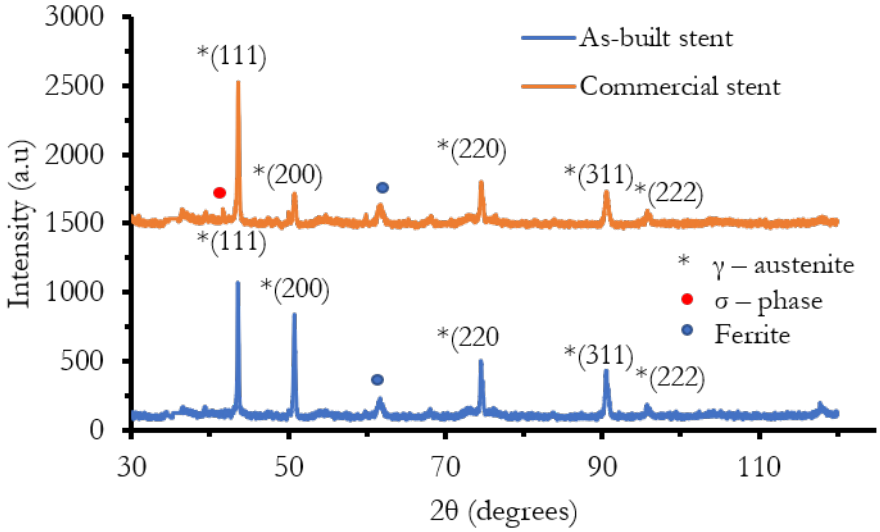

Fig. 5 X-ray diffraction intensity versus 2θ plot for the as-built and commercial stents.

3.3 Microstructure Characterisation

3.3.1 Optical microscopy and SEM

The microstructure, as well as mechanical properties, is known to be affected by the manufacturing method. A comparison of the microstructures of the as-built and commercial stents is shown in Fig. 6 (a) and (b). From optical observation, no cracks or pores were found on polished cross-sections of the as-built and commercial stents. The optical micrograph for the as-built stent showed a clear indication of the melt pools produced from the laser melting of the powder. The melt-pool boundaries (red dotted line) were visible using the optical microscope on the etched sample. Similar to our previous work (Langi *et al.*, 2021), hierarchical structures consisting of

cellular sub-grains inside solidification were also discovered in the present work, especially in the centre of the sample (Fig. 6 (a)). On the other hand, the optical micrograph of the etched commercial stent does not show a complex microstructure, and instead, it had equiaxed grains with the presence of twins (Fig. 6 (b)).

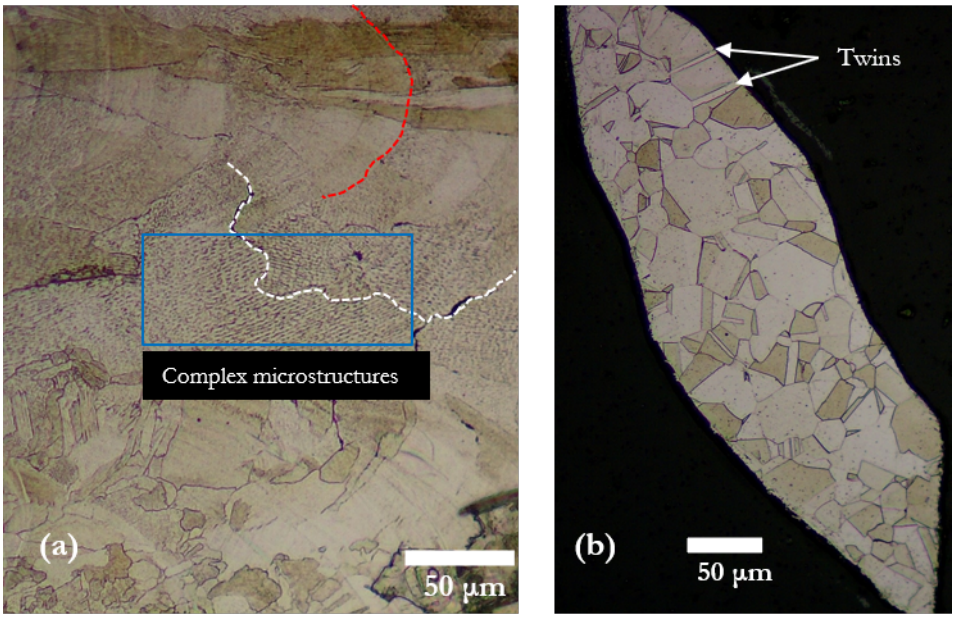

Fig. 6 (a) Optical micrograph of the as-built stent showing complex microstructures, melt pool boundaries (red dotted line) grain boundaries (white dotted line); (b) optical micrograph of the commercial stent with equiaxed grains and twins.

The SEM inspection (Fig. 7) clearly revealed the complex nature of the microstructure for the as-built stent. Under higher magnification, SEM images showed the existence of sub-grain boundaries with different morphologies, i.e., fine, coarse, cellular, and dendritic (Fig. 7 (a)). The grain boundaries were also visible, demonstrating grain variation in size and shape. The differences in the microstructure arise from local changes in temperature gradient (G) and solidification growth rate (R), in which the ratio G/R determines the solidification mode such as columnar dendrite, cellular or equiaxed dendrite, and $G \times R$ or the colling rate dictates the size of the microstructure. The cellular and columnar sub-structure formed in the SLMed 316L SS stent are associated with

the varied solidification process during manufacturing (John C. Lippold, 2015). Basically, the cooling rate towards the edges was higher than that in the middle of the sample, and, as a result, finer microstructures were achieved at the surface. Furthermore, the light cell or dendritic boundaries observed under SEM are sub-grain boundaries that arise due to compositional variation caused by solute redistribution or segregation to the boundaries during solidification of the austenitic stainless steel.

The extent of micro-segregation to the dendrite and cell boundaries was measured using SEM-EDS point scan analysis. A typical SEM-EDS scan is shown in Fig 7 (b), where 1- 8 are the actual points of the scan. A comparison of the chemical composition of the cell boundaries, core regions, and the bulk sample is presented in Table 2. Several measurements were taken at different regions (middle and towards the ends) of the sample and in all cases, a similar trend was observed. The extent of segregation for each element, determined by the ratio of the average amount in the boundaries to its average amount in the core area, is plotted in Fig. 7 (c), which clearly shows that the extent of segregation of Mo to the boundaries is the highest followed by Si and Mn while the extents of Ni and Cr were negligible.

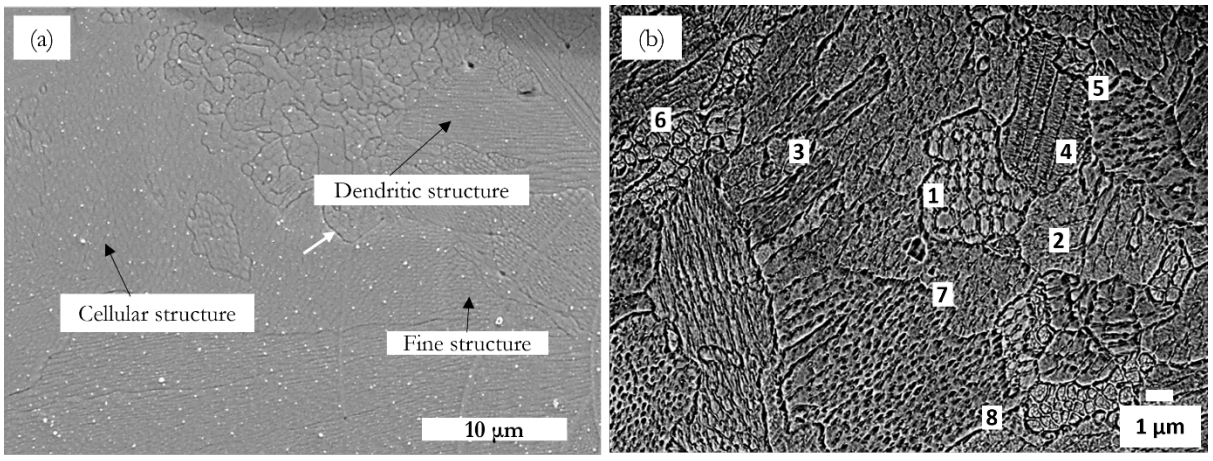

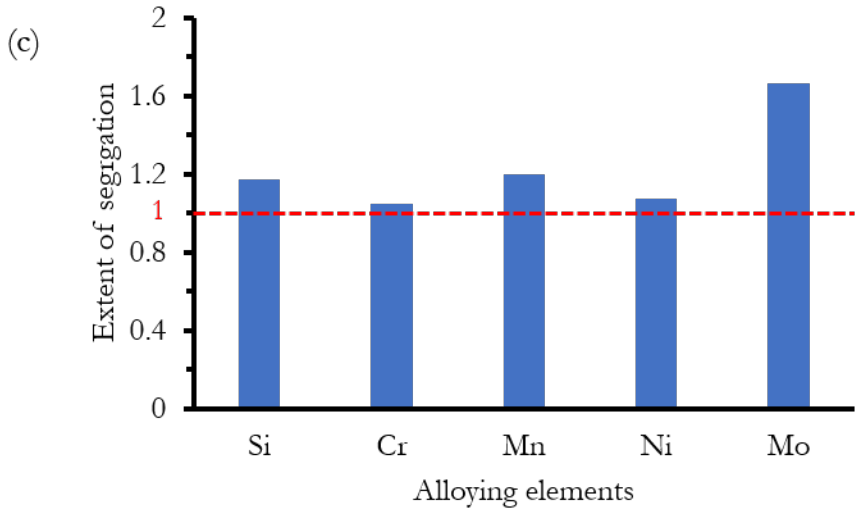

Fig. 7. (a) Higher-resolution SEM images demonstrating microstructural details such as cellular, dendritic, fine, and grain boundary (white arrow); (b) SEM-EDS measurement of microsegregation using scan point analysis; (c) Extent of segregation (the ratio of the average amount in the boundaries to its average amount in the core area).

Table 2: chemical composition in wt% of the cell boundaries, core regions, and the bulk sample

Element	Composition, wt%								
	Core				Boundary				Bulk
	Point 1	Point 2	Point 3	Point 4	Point 5	Point 6	Point 7	Point 8	
Si	0.6	0.5	0.6	0.6	0.7	0.8	0.7	0.5	0.5
Cr	17.5	17.0	17.1	17.4	18.0	17.9	18.2	18.1	17.3
Mn	1.3	1.3	1.2	1.3	1.4	1.5	1.6	1.6	1.3
Ni	12.5	12.0	12.3	12.4	13.1	13.3	13.3	13.3	12.5
Mo	1.5	1.6	1.6	1.5	2.6	2.5	2.6	2.6	1.6

3.3.2 EBSD map

The EBSD maps for both stents are shown in Fig 8 (a) and (b) and the corresponding grain distribution histogram is presented in Fig 8 (c) and (d). For the as-built stent, the microstructures consisted of fine grains towards the edges and coarse grains in the middle (Fig. 8 (a)). The grain size was in the range of 2-110 µm. The long axis of the grains was several hundreds of microns, even larger than the melt pool observed in optical microscopy. There was a widespread in grain size, even in the region with smaller grains. The EBSD data showed that SLM resulted in non-conventional grain shape, orientation, and size, as also reported in other studies (Wang *et al.*, 2018; Mukherjee, 2019). On the other hand, the commercial stent (Fig. 8 (b) consisted of homogeneously distributed equiaxed fine grains, with the grain size in the range 2-50 µm. Apparently, the commercial stent had only a few grains across its strut due to the micron size (100 µm). Furthermore, the commercial stent had twins in its microstructure, suggesting that heat treatment was performed. Other studies (Yan *et al.*, 2014; Agrawal and Singh, 2017) also showed equiaxed grains and twining in 316L SS as a result of grain recrystallisation during the heat treatment process.

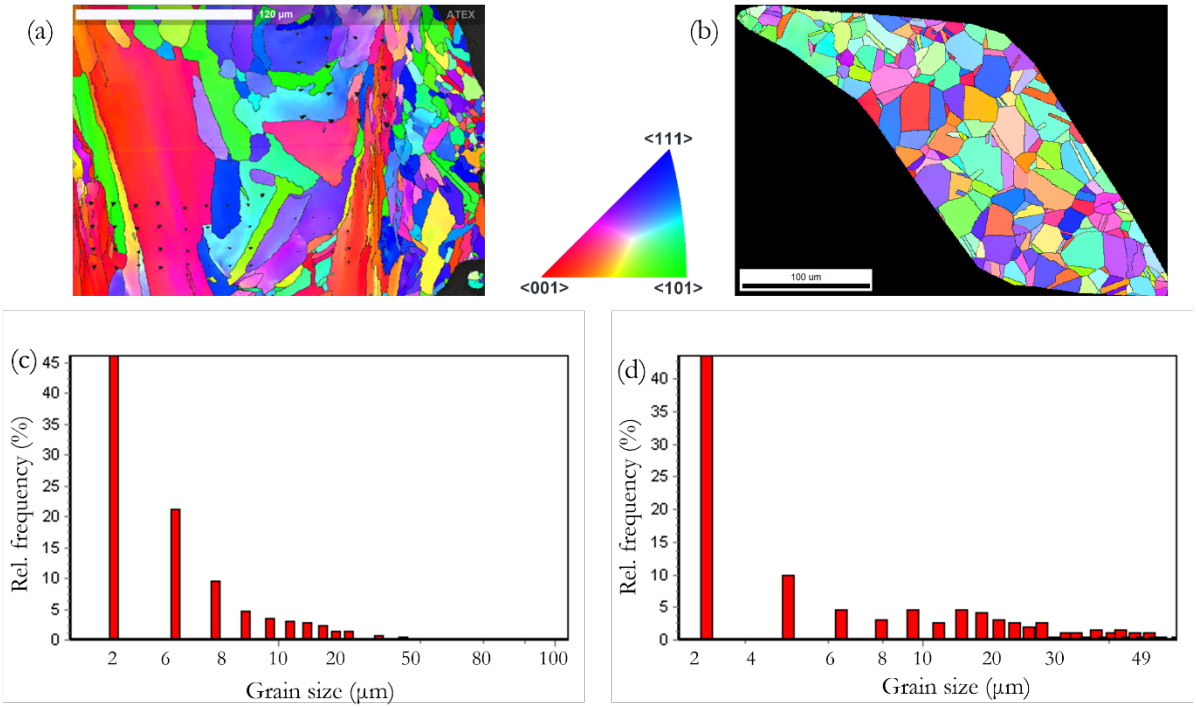

Fig. 8 EBSD maps for (a) as-built and (b) commercial stents in longitudinal cross-section; Grain size histogram for (c) as-built and (d) commercial stents.

3.4 Nanoindentation

3.4.1 Berkovich Nanoindentation

The load-displacement response obtained from Berkovich nanoindentation is shown in Fig. 9 (a) and (b) for tests under 3, 7, 10, 15, and 25 mN. The initial portion of the load-displacement segment was consistent across the different load levels, and the load-displacement response started to differ with the increase in load. All samples exhibited limited load recovery after unloading, indicating severe plastic deformation under Berkovich nanoindentation. The elastic modulus (E) and hardness (H) were calculated from the load-displacement curve using the Oliver and Pharr method, and compared in Fig. 9 (c) and (d) for the five load levels. The as-built stent exhibited hardness in the range of 2.7–3.6 GPa and elastic modulus in the range of 166–210 GPa. On the other hand, the hardness and elastic modulus for the commercial stent was in the range of 2.3–3.2 and 120–180 GPa, respectively. Apparently, the hardness of the as-built stent was higher compared to that of the commercial stent. The higher hardness for the as-built stent can be a result of both solid solution strengthening and dislocation strengthening. Solid solution strengthening is due to the presence of the alloying elements such as carbon and chromium in the alloy, while dislocation strengthening is due to the presence of high density dislocations in the alloy. SLM process is associated with the ultra-fast cooling rate ($10^3 - 10^8 K/s$) during solidification, which results in complex microstructure and finer sub-grains. These features lead to outstanding mechanical properties such as increased hardness and strength for SLMed parts compared with conventionally manufactured parts (Liu *et al.*, 2018; Ma *et al.*, 2017). These strengthening mechanisms explains the enhanced nano-hardness for the as-built stent. The H and E values also reduced with increasing load due to the indentation size effect (Fig. 9 (c) and (d)).

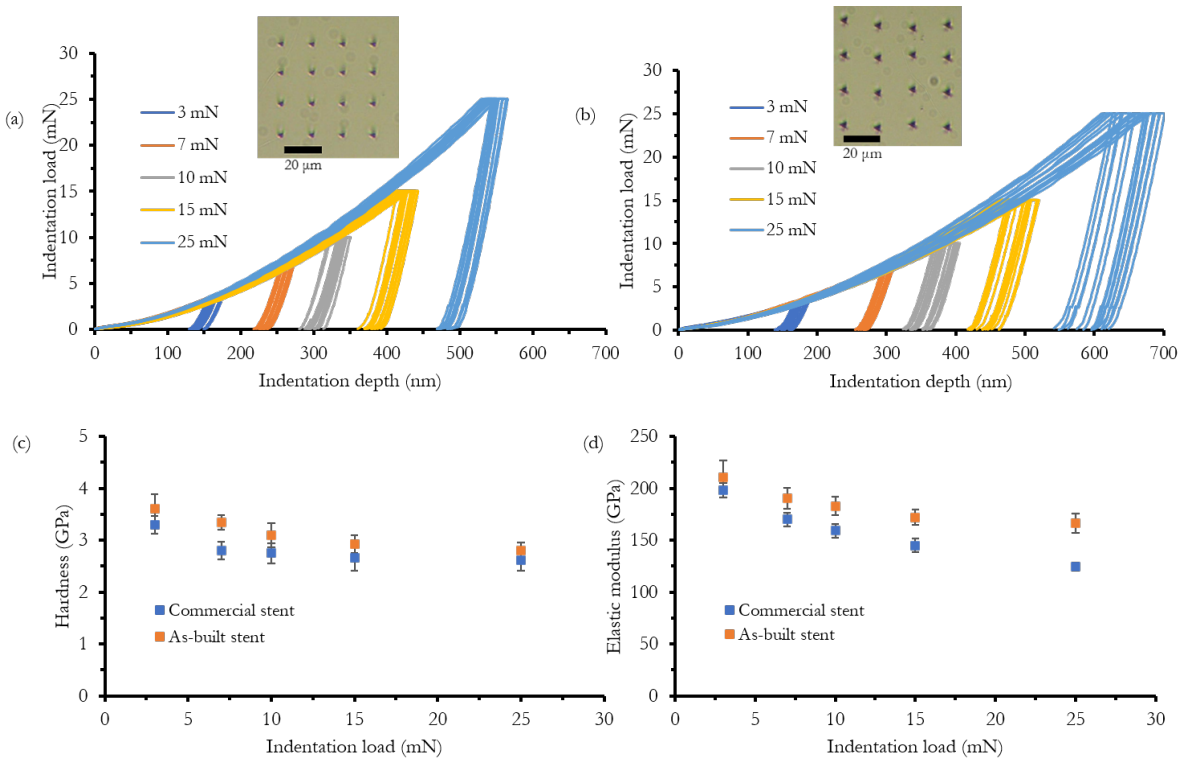

Fig. 9: Load-displacement curves for (a) as-built and (b) commercial stents where the insets show the 4×4 indentation imprints; Variation in (c) hardness and (d) Young's modulus with the load level for as-built and commercial stents.

3.4.2 EBSD analysis after nanoindentation

A spread in the load-displacement curves for indents made at the same load (Fig. 9) suggests that the mechanical response was different at different locations, mostly due to variation of grain orientation. Therefore, the effect of grain orientation on hardness and elastic modulus was investigated by performing EBSD analyses after nanoindentation. Here, we presented the EBSD results for 10 mN load (Fig. 10), where the black triangles indicate the locations of indents.

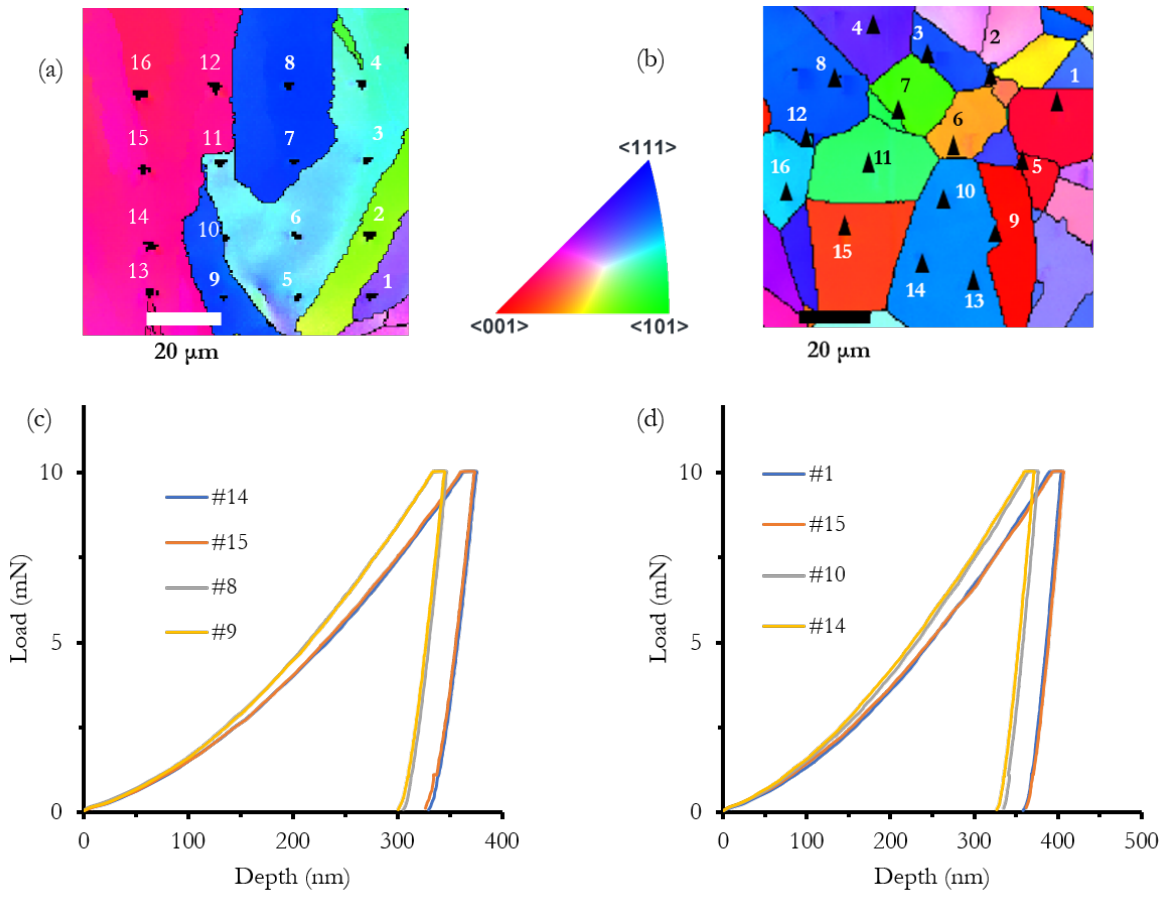

Fig. 10. EBSD maps for imprints made at 10 mN, together with selected load-displacement curves for the as-built (a & c) and commercial (b & d) stents.

For the as-built stent, two indents (#14 and #15) were selected from the grain with a similar orientation (shown in pink); while another two indents (#8 and #9) were selected from a grain (shown in blue) that had a significantly different orientation. The corresponding load-displacement curves for the four indents are shown in Fig. 10 (c), where the initial stage of the load-displacement response coincided for all the four indents, implying close mechanical behaviour within the elastic region. The difference in the load-displacement curves was observed from the elastic-plastic transition up to the peak load. For the indents with similar grain orientation (i.e., #14 and #15; #8 and #9) the difference of load-displacement was almost negligible. However, there was a clear difference in the load-displacement curves between the two indents in the pink grain (#14 and #15) and those two in the blue grain (#8 and #9). For the same load level, a deeper penetration

was obtained for the pink grain when compared to that for the blue grain. The observed differences in penetration were also reported by Chen *et al.*, (2017) and caused by the variaion of the Schmid factor with grain oritentation. Under uniaxial compression, the maximum Schmid factor for (111) orientation was found to be considerably lower than those for (001) and (101) orientation, resulting in higher hardness near (111) orientation. This could explain why at the same load level, a deeper penetration was seen for the indents in the grain near (001) orientation when compared to indents made in the grain near (111) orientation. For all the indentation points, orientation in terms of Bunge–Euler angles were extracted using the HKL Channel 5.0 EBSD postprocessing software. Further, the hardness and elastic modulus were calculated at each indentation point. Table 3 gives a summary of the extracted Bunge–Euler orientation angle (φ1, Φ, φ2), calculated hardness, and the elastic modulus for the as-built and commercial stents. According to Table 3, the hardness and elastic modulus calculated for the as-built stent were higher than those of the commercial stent. Furthermore, the hardness and elastic modulus near (111) orientation was higher than those near (001) orientation.

Table 3: Summary of Bunge–Euler orientation angles (in degrees), hardness, and elastic modulus for selected indents in the as-built and commercial stents under 10 mN load.

Sample	10 mN				
	Indent #	Orientation	Orientation (φ1, Φ, φ2)	H (GPa)	E (GPa)
As-built stent	14	(001)	61.25, 17.59, 46.47	2.82	166.33
	15	(001)	61.59, 19.37, 41.25	2.83	169.59
	8	(111)	97.23, 47.9, 34.21	3.30	194.48
	9	(111)	102.16, 46.7, 34.84	3.35	181.74
	1	(001)	261.15, 10.43, 52.2	2.43	153.14

Commercial stent	15	(001)	327.79, 12.43, 78.84	2.42	148.89
	10	(111)	359.19, 46.93, 28.82	2.84	154.49
	14	(111)	357.35, 47.61, 30.54	2.89	159.60

The elastic modulus and hardness are also plotted in the standard stereographic triangles (SST) (Fig. 11), confirming the effect of grain orientation. Both properties had strong anisotropy depending on the crystallographic orientation, and grains close to (111) orientation had higher elastic modulus and hardness than those close to (001) orientation. Similar results were also found at other load levels which are omitted here to avoid duplications. Basically, the indents performed in the grains near (111) orientation, had the highest hardness and elastic modulus followed by grains near (101) and (001) orientations.

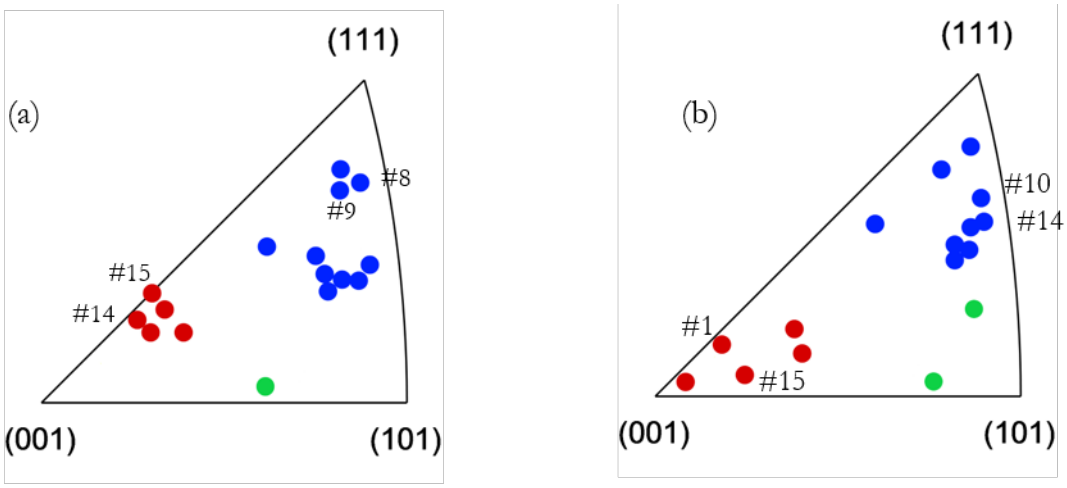

E: 166.33 – 175.76 GPa
H: 2.83 – 2.93 GPa

E: 193.29 GPa
H: 3.05 GPa

E: 181.74 – 194.48 GPa
H: 3.05 – 3.40 GPa

E: 148.89 – 163.95 GPa
H: 2.42 – 2.66 GPa

E: 157.77 – 158.50 GPa
H: 2.71 – 2.90 GPa

E: 164.60 – 178.29 GPa
H: 2.72 – 3.04 GPa

Fig. 11: Hardness and elastic modulus of the grains near (001), (101), and (111) made at 10 mN on SST for (a) as-built stent and (b) commercial stent.

3.5.3 Spherical Nanoindentation

Results so far have shown that nanoindentation tests performed with Berkovich indenter tips were capable of evaluating the mechanical properties in terms of elastic modulus and hardness of the stents. However, such sharp indenter tips are not appropriate when extracting indentation stress-strain curves. This is because the indentation volume beneath the Berkovich indenter tip is dominated by dislocation mediated plasticity with very little elastic deformation. Therefore, spherical nanoindentation was further performed in order to assess the yield strength and hardening behaviour of the stents. In this study, twenty loading and unloading nanoindentation cycles were performed with a minimum and maximum load of 1 and 50 mN, respectively. Representative load-displacement curves for the as-built and commercial stents, indented with spherical nanoindenter tip of diameter 10 μm, are presented in Fig 12 (a) and (b). The inset in Fig. 12 showed that the indents were nearly spherical, and no cracks were observed. It is evident from the load-displacement graphs that the loading-unloading behaviour was consistent for all the indents. Apparently, all the samples experienced significant plastic deformation with very little elastic recovery.

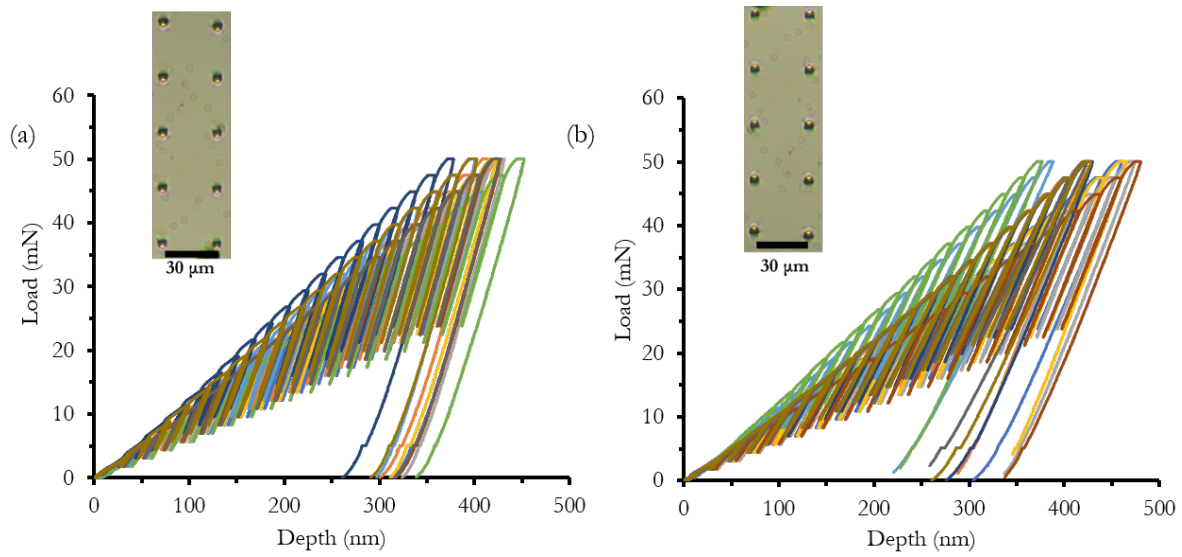

Fig. 12 Load-displacement curves for (a) as-built stent and (b) commercial stent

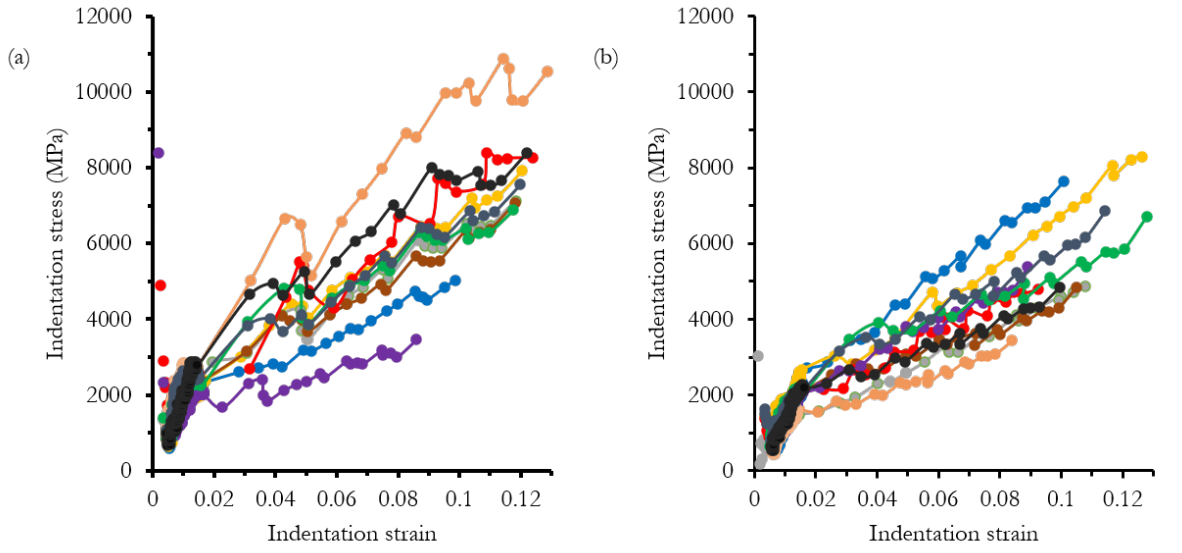

Fig. 13 Representative indentation stress-strain curves for (a) as-built and (b) commercial stents.

Representative indentation stress-strain curves for the samples were calculated from the load-displacement curves and presented in Figure 13 (a) and (b). The crucial point here is to identify the effective initial contact and determination of the contact radius. Here, we followed the method proposed by Pathak and Kalidindi (2015) for the estimation of the effective zero points and the contact radius. Two observations can be made from the representative indentation stress-strain

curves shown in Fig. 13. Firstly, the indentation stress-strain response for the as-built stent was higher than commercial stents. Secondly, both samples demonstrate good consistency within the elastic region and an increased scatter in the plastic region. The as-built stent exhibited more scattering in the plastic region than the commercial stent. This increased scatter can be attributed to several factors in the local microstructures, including dislocating density, sub-grain boundary density, and crystallographic orientations (Chen *et al.*, 2017; Liu *et al.*, 2018). The elastic modulus of the as-built stent and commercial stent, estimated from the elastic part of the curves turn out to be 201.40 ± 9.22 and 190.34 ± 3.13 GPa while the yield strength was 2.4 ± 0.40 and 2.0 ± 0.24 GPa, respectively. The Youngs modulus obtained for the stent matched well with that reported for standard 316L SS, suggesting that the mechanical properties of the samples were adequately captured within the elastic region. Furthermore, nanoindentation yield strength for both samples was nearly a factor of 3.4 larger than that measured from standard uniaxial tensile tests, most likely due to the scale difference.

The indentation stress-strain curves for the samples were further described by the Ramberg–Osgood relationship ($\frac{\varepsilon}{\varepsilon_o} = \frac{\sigma}{\sigma_o} + \alpha(\frac{\sigma}{\sigma_o})^n$), where ε is the total strain, ε_o is the strain at the yield point, σ is the total stress, σ_o is the yield stress, α is the non-dimensional material constant and n is the strain hardening exponent. Here, the Ramberg-Osgood relation was fitted to the representative average stress-strain curves for the two samples (Fig. 14 (a) and (b)), with strain hardening exponent, 4.3 and 3.8, respectively, for the as-built stent and commercial stents.

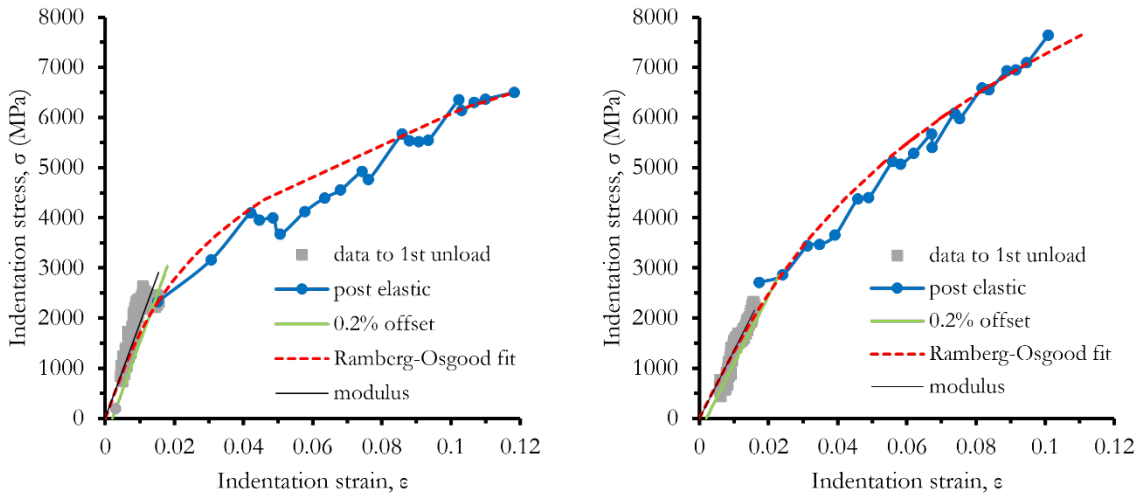

(a)

E_{ind} (GPa)	Y_{ind} (GPa)	n
200.6±9.22	2.24±0.52	4.3

(b)

E_{ind} (GPa)	Y_{ind} (GPa)	n
190.3±3.13	2.02±0.24	3.8

Fig. 14 Indentation stress-strain curves using 10 µm diamond tipped spherical indenter for (a) the as-built (b) commercial stents, showing indentation modulus, E_{ind}, yield stress defied by 0.2 indentation strain offset and Ramberg-Osgood fit

4. Discussions

SLM-based AM process has been attempted to produce metallic stents. However, the full potential of producing metallic stents for the biomedical process is an ongoing endeavour. In this work, a 316L SS stent was fabricated as a first step in understanding surface finish, microstructural and nanomechanical properties of SLMed stents, but with a strut thickness of over 300 µm. Balloon expandable stents produced by laser micromachining have a much smaller structural size (~75–100 µm strut size), presenting a huge challenge for SLM process due to the limitation of current SLM technology. The strut thickness that can be achieved with SLM process depends on several factors such as laser spot size, resolution, and powder size (Demir *et al.,* 2017), and the use of etching can help reduce the strut thickness. Also, stents manufactured by SLM have high surface roughness which needs to be improved through the post-processing process. In this study, electrochemical polishing was found to significantly improve the surface finish of printed stents.

In particular, the average roughness Ra, for the as-built stent decreased from 9.04 µm to 1.53 µm. Although there is still further research to be done for the full potential of SLMed stents to be realised, the results of this study have demonstrated the potential of post-processing techniques such as electrochemical polishing in reducing the average roughness by ~83%. The achieved Ra value was still higher than the expected value of Ra <0.5 µm for biomedical applications. It was also observed that prolonged exposure of etching solution resulted in excessive reduction of the strut size and creation of surface defects.

For cardiovascular application, it is required for the stents to have adequate fatigue strength which can be largely affected by internal pores and sub-surface defects. Results of this work have shown that the printed stent had minimal internal defects and the average area porosity was less than 1% in the optimum condition. In this work, it was ~~totally~~ difficult to eliminate the defects due to the stochastic phenomena that happen during SLM process. The presence of pores is known to affect the fatigue behaviour of the material (Biswal *et al.,* 2018). The pores reduce the time to crack initiation by creating a high-stress concentration region adjacent to the defect. The study by Gong *et al.*, (2015) reported that the presence of pores does not affect the strength and ductility of samples produced by SLM in cases where porosity is maintained to less than 1 vol%. On the contrary, when the size of the pore is in the range of 15 to 600 µm, it can lower strength and ductility due to this microstructural feature where the stress is greater than the surrounding regions. However, the strength of SLMed 316L SS samples is compensated by the presence of a fine sub-grain structure and complex dislocation network formed during ultra-fast cooling. The fine sub-grain structure can hinder dislocation motion (Liu *et al.*, 2018), leading to increased strength and ductility in 316L SS parts produced by SLM. Furthermore, the surface post-processing techniques such as laser shock peening (LSP), shot peening (SP), ultrasonic shot peening (USP), ultrasonic impact treatment (UIT), and barrel finishing (BF) can also be applied to additively manufactured parts (Chan *et al.*, 2010; Boschetto *et al.,* 2015; Dekhtyar *et al.*, 2015; Karthik et *al.,* 2017; Zaleski *et*

al., 2017). These techniques can modify the near-surface layers leading to surface microrelief, compressive residual macro-stress, and increased surface hardness, though it is a challenging task for a stent due to its complex form.

In general, the results of this study depict that the microstructures and nanomechanical properties were affected by SLM process. During SLM, a high-power laser beam fuses metallic powder, which then forms a melt pool, leading to the cooling rate in the range of 10^3 to 10^8 K/s. As a result, the microstructures of the as-built stent consisted of coarse and columnar grains in the middle of the sample with complex microstructure and sub-grains structures with grains size less than 3 μm. On the contrary, the optical micrograph of the commercial stent did not show the complex microstructure observed in the as-built stent. The commercial stent had an average grain size of 20 μm. Currently, for metallic stents with strut thickness in the range of 50-140 μm, equiaxed grains (e.g., size of 5-10 μm) across their thickness are desirable microstructures. Stents with thinner struts have been reported to have both mechanical and clinical benefits such as an increase in stent flexibility, decrease in pressure needed for deployment, and reduction in in-stent restenosis rate (Obayi *et al.*, 2016). -Furthermore, it is required for stents to have a good combination of radial strength and ductility. In normal operation, stents need adequate fatigue strength to withstand many millions of pulsations from the artery. Grain microstructure is a key microstructural feature that can affect the mechanical behaviour of the stent. For most polycrystalline materials, the mechanical properties increase with a decrease in the grain size according to the Hall Petch relationship (Obayi *et al.*, 2016). While, for single-phase metals, it has also been reported that a decrease in the average grain size leads to a decrease in ductility (Song *et al.*, 2006). However, the behaviour of micron-scale stent strut has been found sensitive to grain microstructure which could be optimised by heat treatment process (Murphy *et al.*, 2006).

Given the advantage of complex microstructure, the stent produced by SLM showed higher hardness and modulus than a commercial stent, which confirms the significant effect of microstructures on the mechanical properties of the printed stent. The improvement in hardness and modulus can be attributed to impediment of dislocation motion due to fine sub-grain structure in the SLMed stent. Heat treatment, in particular solution annealing, may be required to further tune the hardness– (Murphy *et al.*, 2006). The other benefit of heat treatment is improving the mechanical behaviour of the stents by stress relieving, providing equiaxed grains, and improving ductility. Despite the observed difference in the microstructures, indentation stress-strain curves for the printed and commercial stents were comparable. Since most of the indents were probing within the grain, it can be argued that grain size and morphology did not have a significant effect on the indentation yield strength and stress-strain curve. However, further uniaxial tensile tests on mini dog-bone samples with a width similar to the strut thickness are underway to gain further understanding of the effect of grain microstructure on stress-strain response.

This paper provides a comparative study of microstructures and nanomechanical properties of additively manufactured and commercial metallic stents, which is useful for the potential adoption of AM in patient-specific, individualised (?) stent production. Results have shown that the grain microstructure of SLMed stent will need to be optimized (i.e., through heat treatment), to further improve the mechanical properties required for stents such as strength and ductility. It is also necessary to further reduce the strut size (currently three times thicker than commercial ones) during the SLM process in future research, to compete with the thin strut structure of commercial stents. Thin struts will improve the stent flexibility, reduce the cross-sectional profiles, and decrease the pressure needed for deployment. In addition, the thinner struts reduce the rate of in-stent restenosis significantly and are associated with faster re-endothelialisation when compared to thicker struts. It must also be noted that although only microstructure and mechanical properties were studied, future work will include a more comprehensive analysis of stent performance such

as crimping, expansion recoil and fatigue resistance behaviour. Overall, this work provides insights into the microstructure and properties of additively manufactured stents, and represents an important step towards innovative manufacturing of future stents using AM.

4. Conclusions

This work reports the surface finish, electrochemical polishing, underlying microstructure, and mechanical properties of both SLMed and commercial stents. The main findings are:

- Electrochemical polishing is effective in reducing the average roughness value (Ra) by approximately 83 %. However, further reduction in surface roughness needs to be achieved by combining mechanical grinding with electro and plasma polishing and blasting using different grits.
- The microstructure of the as-built stent consisted of hierarchical microstructure, consisting of cellular sub-grain structures and columnar grain structures, as opposed to equiaxed fine grains in the commercial stent. Results suggest that the grain microstructures of the SLMed stent can be further optimised to improve the mechanical properties required for stents.
- The hardness of the as-built stent is higher than that of the commercial stent, which is likely due to the increased dislocation density, finer sub-grains, and complex microstructures caused by the ultra-fast cooling rate during solidification.
- The indentation stress-strain curves for the as-built stent and commercial stent were close to each other. Furthermore, nanoindentation-determined yield strength for both samples appears to be nearly a factor of 3.4 larger than that measured from bulk uniaxial tensile tests.
- Both hardness and Young's modulus demonstrated a distinct grain orientation dependency; In particular, the indents close to (111) orientation exhibited the highest levels of hardness and elastic modulus followed by (101) and then (001) orientations.

5. Acknowledgments

We acknowledge the support from the EPSRC UK (Grant number: EP/R001650/1; Title: Smart peripheral stents for the lower extremity - design, manufacturing, and evaluation). Research data for this paper are available upon request to the project's principal investigator Professor Liguo Zhao at Loughborough University, UK (email: L.Zhao@lboro.ac.uk).

6. References

Agrawal, A. K. and Singh, A. (2017) 'Limitations on the hardness increase in 316L stainless steel under dynamic plastic deformation', *Materials Science and Engineering* , 687, pp. 306–312. doi: 10.1016/j.msea.2017.01.066.

Biswal, R., Syed, A. K. and Zhang, X. (2018) 'Assessment of the effect of isolated porosity defects on the fatigue performance of additive manufactured titanium alloy', *Additive Manufacturing.* , 23, pp. 433–442. doi: 10.1016/j.addma.2018.08.024.

Boschetto, A., Bottini, L. and Sapienza, L. (2015) 'Surface improvement of fused deposition modeling parts by barrel finishing', *Rapid Prototyping Journal*, 6, pp. 686–696. doi: 10.1108/RPJ-10-2013-0105.

Chan, H. L. *et al.* (2010) 'Optimization of the strain rate to achieve exceptional mechanical properties of 304 stainless steel using high speed ultrasonic surface mechanical attrition treatment', *Acta Materialia*, 58, pp. 5086–5096. doi: 10.1016/j.actamat.2010.05.044.

Chen, T. *et al.* (2017) 'The effect of grain orientation on nanoindentation behavior of model austenitic alloy Fe-20Cr-25Ni', *Acta Materialia.*, 138, pp. 83–91. doi: 10.1016/j.actamat.2017.07.028.

Dekhtyar, A. I. *et al.* (2015) 'Enhanced fatigue behavior of powder metallurgy Ti – 6Al – 4V alloy by applying ultrasonic impact treatment', *Materials Science & Engineering A.* , 641, pp. 348–359. doi: 10.1016/j.msea.2015.06.072.

Demir, A. G. and Previtali, B. (2017) 'Additive manufacturing of cardiovascular CoCr stents by

selective laser melting', *Materials and Design*, 119, pp. 338–350. doi: 10.1016/j.matdes.2017.01.091.

Finazzi, V. *et al.* (2020) 'Design and functional testing of a novel balloon-expandable cardiovascular stent in CoCr alloy produced by selective laser melting', *Journal of Manufacturing Processes*, 55, pp. 161–173. doi: 10.1016/j.jmapro.2020.03.060.

Gong, H. *et al.* (2015) 'Influence of defects on mechanical properties of Ti-6Al-4V components produced by selective laser melting and electron beam melting', *Materials and Design*, 86, pp. 545–554. doi: 10.1016/j.matdes.2015.07.147.

Guerra, A. J. and Ciurana, J. (2018) '3D-printed bioabsordable polycaprolactone stent: The effect of process parameters on its physical features', *Materials and Design*., 137, pp. 430–437. doi: 10.1016/j.matdes.2017.10.045.

Jia, H., Gu, S. Y. and Chang, K. (2018) '3D printed self-expandable vascular stents from biodegradable shape memory polymer', *Advances in Polymer Technology*, 37(8), pp. 3222–3228. doi: 10.1002/adv.22091.

John C. Lippold (2015) 'Effect of Microstructure', in *Welding Metallurgy and Weldability*. Hoboken, New Jersey: John Wiley & Sons, Inc., pp. 224–262.

Karthik, D. and Swaroop, S. (2017) 'Laser shock peening enhanced corrosion properties in a nickel based Inconel 600 superalloy', *Journal of Alloys and Compounds*., 694, pp. 1309–1319. doi: 10.1016/j.jallcom.2016.10.093.

Langi, E. *et al.* (2020) 'Microstructural and Mechanical Characterization of Thin-Walled Tube Manufactured with Selective Laser Melting for Stent Application', *Journal of Materials Engineering and Performance*. . doi: 10.1007/s11665-020-05366-9.

Langi, E. *et al.* (2021) 'Microstructural and Mechanical Characterization of Thin-Walled Tube Manufactured with Selective Laser Melting for Stent Application', *Journal of Materials Engineering and Performance*. doi: 10.1007/s11665-020-05366-9.

Liu, L. *et al.* (2018) 'Dislocation network in additive manufactured steel breaks strength–ductility trade-off', *Materials Today*., 21(4), pp. 354–361. doi: 10.1016/j.mattod.2017.11.004.

Löber, L. *et al.* (2013) 'Comparison of different post processing technologies for SLM generated 316l steel parts', *Rapid Prototyping Journal*, 19(3), pp. 173–179. doi: 10.1108/13552541311312166.

Ma, M., Wang, Z. and Zeng, X. (2017) 'A comparison on metallurgical behaviors of 316L stainless steel by selective laser melting and laser cladding deposition', *Materials Science and Engineering A.* , 685, pp. 265–273. doi: 10.1016/j.msea.2016.12.112.

Mcgee, O. M. *et al.* (2021) 'An Investigation into Patient-Specific 3D Printed Titanium Stents and the use of Etching to Overcome Selective Laser Melting Design Constraints .', *Cold Spring Harbor Laboratory*. Available at: https://www.biorxiv.org/content/10.1101/2021.03.07.434132v1.

Michael Bünger, C. *et al.* (2007) 'Sirolimus-Eluting Biodegradable Poly-l-Lactide Stent for Peripheral Vascular Application: A Preliminary Study in Porcine Carotid Arteries', *Journal of Surgical Research*, 139(1), pp. 77–82. doi: 10.1016/j.jss.2006.07.035.

Moore, S. S., O'Sullivan, K. J. and Verdecchia, F. (2016) 'Shrinking the Supply Chain for Implantable Coronary Stent Devices', *Annals of Biomedical Engineering*, 44(2), pp. 497–507. doi: 10.1007/s10439-015-1471-8.

Mukherjee, M. (2019) 'Effect of build geometry and orientation on microstructure and properties of additively manufactured 316L stainless steel by laser metal deposition', *Materialia*, 7(May), pp. 5–8. doi: 10.1016/j.mtla.2019.100359.

Murphy, B. P. *et al.* (2006) 'The influence of grain size on the ductility of micro-scale stainless steel stent struts', *Journal of Materials Science: Materials in Medicine*, 17(1), pp. 1–6. doi: 10.1007/s10856-006-6323-5.

Obayi, C. S. *et al.* (2016) 'Effect of grain sizes on mechanical properties and biodegradation behavior of pure iron for cardiovascular stent application', *Biomatter.*, 6, p. e959874. doi: 10.4161/21592527.2014.959874.

Oliver, W. C. and Pharr, G. M. (1992) 'An improved technique for determining hardness and elastic modulus using load and displacement sensing indentation experiments', *Journal of Materials Research*, 7(6), pp. 1564–1583.

Patel, D. K. and Kalidindi, S. R. (2016) 'Correlation of spherical nanoindentation stress-strain curves to simple compression stress-strain curves for elastic-plastic isotropic materials using finite element models', *Acta Materialia*, 112, pp. 295–302. doi: 10.1016/j.actamat.2016.04.034.

Pathak, S. and Kalidindi, S. R. (2015) 'Spherical nanoindentation stress-strain curves', *Materials Science and Engineering R: Reports*. 91, pp. 1–36. doi: 10.1016/j.mser.2015.02.001.

Pathak, S., Shaffer, J. and Kalidindi, S. R. (2009) 'Determination of an effective zero-point and extraction of indentation stress – strain curves without the continuous stiffness measurement signal', *Scripta Materialia*. 60(6), pp. 439–442. doi: 10.1016/j.scriptamat.2008.11.028.

Saeidi, K., Gao, X., Zhong, Y., *et al.* (2015) 'Hardened austenite steel with columnar sub-grain structure formed by laser melting', *Materials Science and Engineering A*. 625, pp. 221–229. doi: 10.1016/j.msea.2014.12.018.

Saeidi, K., Gao, X., Lofaj, F., *et al.* (2015) 'Transformation of austenite to duplex austenite-ferrite assembly in annealed stainless steel 316L consolidated by laser melting', *Journal of Alloys and Compounds*. 633, pp. 463–469. doi: 10.1016/j.jallcom.2015.01.249.

Schmidt, W. *et al.* (2002) 'Characteristic mechanical properties of balloon-expandable peripheral stent systems', *Advances in X-Rays and Imaging*, 174(11), pp. 1430–1437. doi: 10.1055/s-2002-35345.

Song, R. *et al.* (2006) 'Overview of processing, microstructure and mechanical properties of ultrafine grained bcc steels', *Materials Science and Engineering A*, 441(1–2), pp. 1–17. doi: 10.1016/j.msea.2006.08.095.

Wang, X. *et al.* (2018) 'Microstructure and mechanical properties of stainless steel 316L vertical struts manufactured by laser powder bed fusion process', *Materials Science and Engineering A*. 736, pp. 27–40. doi: 10.1016/j.msea.2018.08.069.

Wessarges, Y. *et al.* (2014) 'Additive manufacturing of vascular implants by selective laser melting', in *Biomedizinische Technik*, pp. S401–S404. doi: 10.1515/bmt-2014-5005.

Yan, F. K. *et al.* (2014) 'Deformation mechanisms in an austenitic single-phase duplex microstructured steel with nanotwinned grains', *Acta Materialia*, 81, pp. 487–500. doi:

10.1016/j.actamat.2014.08.054.

Yin, Y. J. *et al.* (2019) 'Mechanism of high yield strength and yield ratio of 316 L stainless steel by additive manufacturing', *Materials Science and Engineering A.*, 744, pp. 773–777. doi: 10.1016/j.msea.2018.12.092.

Zaleski, K. and Skoczylas, A. (2017) 'The Effect of the Conditions of Shot Peening the Inconel 718 Nickel Alloy on the Geometrical Structure of the Surface', *Advances in Science and Technology*, 11(1), pp. 205–211. doi: 10.12913/22998624/74180.

Zhou, X. *et al.* (2015) '3D-imaging of selective laser melting defects in a Co-Cr-Mo alloy by synchrotron radiation micro-CT', *Acta Materialia.*, 98, pp. 1–16. doi: 10.1016/j.actamat.2015.07.014.